

Absorption Measure Distribution of the Outflow in IRAS 13349+2438: Direct Observation of Thermal Instability?

Tomer Holczer ¹, Ehud Behar ¹ and Shai Kaspi ^{1,2}

ABSTRACT

We analyze the *Chandra* X-ray spectrum obtained with the HETGS grating spectrometer of IRAS 13349+2438, which has one of the richest absorption spectra of a quasar outflow. Absorption from almost all charge states of Fe is detected. This allows for a detailed reconstruction of the absorption measure distribution (*AMD*), which we define as the continuous distribution of column density as a function of ionization parameter. We find a double peaked *AMD* for IRAS 13349+2438 with a total (ionized) column density of $N_H = (1.2 \pm 0.3) \times 10^{22} \text{ cm}^{-2}$ assuming solar iron abundance. For comparison, we perform a similar analysis on the well studied HETGS spectrum of NGC 3783. Both sources feature a deep minimum in column density consistent with no absorption from gas at temperatures of $4.5 < \log T < 5$ (K). We interpret the minima as observational evidence for thermal instability in this temperature regime.

Subject headings: galaxies: active — galaxies: individual (IRAS 13349+2438, NGC 3783) — techniques: spectroscopic — X-rays: galaxies — line: formation

1. INTRODUCTION

The X-ray spectra of many active galactic nuclei (AGNs) viewed directly toward the central source (e.g., Seyfert 1 galaxies) show the continuum flux absorbed by numerous absorption lines produced by ionized gas. The lines are generally shifted to shorter wavelengths, indicating an outflowing wind. It is not clear whether this wind can also be associated with the line-of-sight material responsible for the optical reddening of these sources. To that end, the outflow would have to entail neutral- gas or dust grains along with the highly ionized

¹Department of Physics, Technion, Haifa 32000, Israel. tomer@physics.technion.ac.il (TH), behar@physics.technion.ac.il (EB), shai@physics.technion.ac.il (SK).

²School of Physics and Astronomy, Raymond and Beverley Sackler Faculty of Exact Sciences, Tel Aviv University, Tel-Aviv, 69978 ISRAEL

wind. It is still controversial whether the winds are significant for the AGN central engine or for the host galaxy in terms of mass, energy, and momentum. It is possible that extreme outflows may even play a central role in cosmological feedback and in the metal enrichment of the intergalactic medium (IGM). In order to address these open questions, it is important to develop reliable techniques to probe the winds and to perform accurate measurements of their physical properties.

The X-ray band is advantageous for AGN outflow studies not only because most of the outflow appears to be highly ionized, but also since the X-ray band comprises detectable absorption lines from the full range of charge states: From neutral up to hydrogen-like. Moreover, in most cases an X-ray spectrum features several lines from a single ion, which helps to deduce ionic column densities from saturated absorption lines. The detection of many charge states of a single element is key to plasma diagnostics as it allows to model the distribution of ionization and to measure the total column density independent of assumptions regarding the relative element abundances. For this purpose, Fe ions are particularly useful as they form over several orders of magnitude of the ionization parameter, defined (e.g., Kallman & Krolik 1995) by

$$\xi = \frac{L}{n_H r^2} \quad (1)$$

where L is the ionizing luminosity between 1 and 1000 Rydberg, n_H denotes the hydrogen number density and r is the distance of the absorber from the ionizing source. Once the distribution of ionization is known for one element, the relative abundances of other elements can be measured by comparison. For the absolute abundances of metals with respect to hydrogen, one still needs to utilize UV spectra, as the energies of atomic transitions in hydrogen are too low to be observed in the X-rays. Highly ionized K- and L- shell ions (1-2, and 3-10 electrons, respectively) of Fe appear regularly in astrophysical X-ray sources, either in emission or in absorption. The lower charge states of Fe (11-26 electrons) feature strong inner-shell absorption lines in the soft X-ray band (Behar et al. 2001). Each ion can produce dozens of overlapping lines forming unresolved transition arrays (UTAs). Interestingly, IRAS 13349+2438 was the first source in which Fe M-shell UTAs were observed (Sako et al. 2001).

The majority of works on the X-ray spectra of AGN outflows fit the data with a gradually increasing number of iso- ξ absorption components, until the fit is satisfactory (e.g., Kaspi et al. 2001; Kaastra et al. 2002; Netzer et al. 2003). For high-quality spectra two or three ionization components produce a good fit. In this work, we employ a more fundamental method, which tries to reconstruct the actual distribution of the column density in

the plasma as a continuous function of ξ . We call this distribution the absorption measure distribution (*AMD*). The present method is similar in principle to that tested by Steenbrugge et al. (2005) and by Costantini et al. (2007), who assumed a power-law distribution. However, here we fit for the *AMD* directly from the measured ionic column densities making no *a-priori* assumptions regarding its shape.

IRAS 13349+2438 is a bright type-1 quasar ($L > 10^{46}$ erg s $^{-1}$) at a redshift of $z=0.10764$ (Kim et al. 1995). Optical and infrared observations by Wills et al. (1992) have suggested absorption of the central source by dust. X-ray observations with *ROSAT* (Brandt et al. 1996) and *ASCA* (Brandt et al. 1997) did not find a significant column density of cold material, but suggested the presence of ionized gas along the line of sight, perhaps with embedded dust grains. Siebert et al. (1999) restated the difficulty to explain the optical and X-ray observations with the same absorber. The line-resolved RGS (Reflection Grating Spectrometer on board *XMM-Newton*) spectrum of IRAS 13349+2438 measured by Sako et al. (2001) revealed broad (FWHM $\simeq 1400 \pm 300$ km s $^{-1}$) absorption lines of many ions. Two distinct ionization components were determined at $\log \xi \simeq 0$ and at $\log \xi \simeq 2 - 2.5$ where ξ is in c.g.s. units (erg cm s $^{-1}$). The low- and high- ξ components were found to have column densities of a few 10^{21} cm $^{-2}$ and a few 10^{22} cm $^{-2}$, respectively. The good agreement between the low- ξ column density and that deduced from the optical reddening (Wills et al. 1992) led Sako et al. (2001) to conjecture that the low- ξ absorber might be responsible also for the optical reddening. In this paper, we revisit the ionized absorber of IRAS 13349+2438 using a long exposure with the High Energy Transmission Grating (HETGS) spectrometer on board *Chandra* performed 3 years and 9 months after the *XMM-Newton* observation. The spectral resolution of HETGS is much better than that of the RGS and the long exposure compensates for its inferior effective area.

2. DATA REDUCTION

IRAS 13349+2438 was observed by *Chandra*/HETGS on 22–26 February, 2004 for a total exposure time of 300 ks. All observations were reduced from the *Chandra* archive using the standard pipeline software (CIAO version 3.2.1). The total number of counts in the first (plus and minus) orders between 2 and 20 Å is 22836 for MEG (medium energy grating) and 9542 for HEG (high energy). No background subtraction was required as the background level was negligible. The post-pipeline procedure is similar to the method reported in Kaspi et al. (2001). Flux spectra were obtained by dividing the count spectra by the effective area curves produced by the standard CIAO tool. Positive and negative first-order data of both the MEG and HEG instruments were combined. The spectrum was corrected for neutral

galactic absorption ($N_H = 1.1 \times 10^{20} \text{ cm}^{-2}$, Murphy et al. 1996). The data were rebinned to 36 mÅ bins to improve the statistics of the spectra with minimal compromise of the spectral resolution, as the MEG instrumental line spread function is approximately 23 mÅ broad (FWHM).

3. SPECTRAL MODEL

Variations of approximately 25% on time scales of 20 ks were observed during the 300 ks exposure of IRAS 13349+2438. Due to this low level of variability and since we are interested in the over all properties of the ionized absorber, henceforth, we use only the combined MEG and HEG full 300 ks spectrum. The present fitting procedure follows our ion-by-ion fitting method (Behar et al. 2001, 2003; Holczer et al. 2005). First, we fit for the broad-band continuum. Subsequently, we fit the absorption features using template ionic spectra that include all of the absorption lines and photoelectric edges of each ion, but vary with the broadening (so-called turbulent) velocity and the ionic column density.

3.1. Continuum Parameters

The continuum spectrum of IRAS 13349+2438 can be characterized by a high-energy power-law and a blackbody that rises at lower energies. The present best-fit power-law parameters are a photon index of $\Gamma_\epsilon = 1.9$ with a total flux in the 5–35 Å range of $2.8 \times 10^{-3} \text{ photons cm}^{-2} \text{ s}^{-1}$, to be compared to $\Gamma_\epsilon = 2.2$ and a flux of $2.4 \times 10^{-3} \text{ photons cm}^{-2} \text{ s}^{-1}$ obtained by Sako et al. (2001). The current blackbody has a temperature of $kT = 105 \text{ eV}$ and a 5–35 Å flux of $7.8 \times 10^{-3} \text{ photons cm}^{-2} \text{ s}^{-1}$, compared to $kT = 100 \text{ eV}$ and $4.0 \times 10^{-3} \text{ photons cm}^{-2} \text{ s}^{-1}$ obtained by Sako et al. (2001). The continuum applied by Brandt et al. (1997) to the *ASCA* data produced a flux in the 2–10 keV range of $5.7 \times 10^{-12} \text{ erg cm}^{-2} \text{ s}^{-1}$ compared to the present value of $3.6 \times 10^{-12} \text{ erg cm}^{-2} \text{ s}^{-1}$. The continuum applied by Brandt et al. (1996) to the *ROSAT* data produced a flux in the 0.1–2.5 keV range of $1.2 \times 10^{-11} \text{ erg cm}^{-2} \text{ s}^{-1}$ compared to the present value of $1.7 \times 10^{-11} \text{ erg cm}^{-2} \text{ s}^{-1}$. In short, the continuum measured here with *Chandra* is within $\sim 50\%$ of all previous observations. In particular, the continuum model parameters are fairly similar to those of Sako et al. (2001). In Fig. 1 we present a direct comparison of the two grating spectra from these two observations showing their over all similarity. It can be seen that the hard X-ray flux is almost identical, while there is some increase in the soft flux. This change is reflected in the small difference between the two models in the blackbody normalization parameters. One might notice that the depth of the O K-shell edges is also different between observations.

This is discussed in more detail below in §4.1.

3.2. The Ionized Absorber

The spectrum $I_{ij}(\nu)$ around an atomic absorption line $i \rightarrow j$ can be represented by:

$$I_{ij}(\nu) = I_0(\nu) \exp [-N_{ion}\sigma_{ij}(\nu)] \quad (2)$$

where $I_0(\nu)$ represents the continuum intensity, $\sigma_{ij}(\nu)$ denotes the line absorption cross section for photoexcitation (in cm^2) from ground level i to level j . If all ions are essentially in the ground level. N_{ion} is the total ionic column density towards the source in cm^{-2} . The photoexcitation cross section is given by:

$$\sigma_{ij}(\nu) = \frac{\pi e^2}{m_e c} f_{ij} \phi(\nu) \quad (3)$$

f_{ij} denotes the absorption oscillator strength and $\phi(\nu)$ represents the Voigt profile due to the convolution of natural (Lorentzian) and Doppler (Gaussian) line broadening. The Doppler broadening consists of thermal and turbulent motion, but in AGN outflows, the turbulent broadening appears to totally dominate the temperature broadening. Transition wavelengths, natural widths and oscillator strengths were calculated using the Hebrew University Lawrence Livermore Atomic Code (HULLAC, Bar-Shalom et al. 2001). More recent and improved atomic data for the Fe M-shell ions were incorporated from Gu et al. (2006).

The Doppler broadening can be typically characterized by a turbulent velocity v_{turb} , although for very high resolution UV spectra of AGN outflows, this approximation has been shown to be inadequate and velocity-dependent partial covering effects need to be taken into account (Arav et al. 1999). Due to the limited resolution, the present HETGS spectrum of IRAS 13349+2438 does not warrant a more sophisticated analysis than the v_{turb} approximation. Indeed, a turbulent velocity of $v_{turb} = 640 \text{ km s}^{-1}$, corresponding to a FWHM of $\sim 1500 \text{ km s}^{-1}$, provides a good fit to the strongest absorption lines in the spectrum as demonstrated in Fig. 2 for the Fe^{+16} absorption line at 15.01 \AA . This specific absorption line is shown because it has a high oscillator strength of 2.3 and it is relatively unblended. The value of $v_{turb} = 640 \text{ km s}^{-1}$ is consistent with that quoted by Sako et al. (2001).

Since the absorbing gas is outflowing, the absorption lines are slightly blue-shifted with respect to the AGN rest frame. The current best-fit outflow velocity is $-300 \pm 50 \text{ km s}^{-1}$. Errors correspond to $\Delta\chi^2 = 1$. Sako et al. (2001), on the other hand, found from the RGS

spectrum two velocity components, high- and low- ionization components with velocities of $+20^{+330}_{-200}$ km s⁻¹, and -420^{+180}_{-190} km s⁻¹, respectively. We find that a single outflow velocity of -300 ± 50 km s⁻¹ actually provides a better fit to the HETGS spectrum. In Fig. 2, the centroid of the Fe⁺¹⁶ line can be seen to be offset from the zero-velocity position by at least six sigma ($\sigma = 50$ km s⁻¹). Sako et al. (2001) ascribed this line to the high-ionization component with $v_{out} = +20^{+330}_{-200}$ km s⁻¹. The -300 km s⁻¹ blue-shift (obtained by fitting *all* absorption lines in the spectrum simultaneously) clearly provides a better fit to the profile of this specific line. We ascribe the potential discrepancy with Sako et al. (2001) to the superior spectral resolution of the present HETGS measurement and to the large errors on the velocities of Sako et al. (2001). If anything, the data in Fig. 2 hint at an even higher velocity for this specific line, which might suggest that there is some scatter in velocity between the different ions. However, this effect is too weak for us to measure even with HETGS and henceforth, we assume a uniform outflow velocity of -300 ± 50 km s⁻¹.

Our model includes all of the important lines of all ion species that can absorb in the waveband observed by HETGS. In the present spectrum of IRAS 13349+2438, we find evidence for the following ions: N⁺⁶, all charge states of O, Ne⁺⁶–Ne⁺⁹, Mg⁺⁴–Mg⁺¹¹, Na⁺¹⁰, Si⁺⁵–Si⁺¹³, 21 ions of Fe, and Ni⁺¹⁸. We also include the K-shell photoelectric edges for all these ions although their effect here is largely negligible. When fitting the data, each ionic column density is treated as a free parameter. A preliminary fit is obtained using a custom made Monte-Carlo fitting method applied to the entire spectrum. Subsequently, the final fit is obtained for individual ionic column densities in a more controlled manner, which ensures that the fit of the leading lines is not compromised. The best fit model for the present spectrum of IRAS 13349+2438 is shown in Fig. 3. It can be seen that the Si, Mg, Ne, and Fe L-shell lines are reproduced fairly well by the model. However, in the Fe M-shell region between 15.0 – 17.5 Å, the spectrum is rather noisy and it is difficult to identify individual ions. For these ions, only rough estimates of the column densities can be obtained. Note that some lines could be saturated, e.g., the leading lines of O⁺⁶ and O⁺⁷. In these cases, the higher order lines with lower oscillator strengths are crucial for obtaining reliable N_{ion} values.

4. IONIC COLUMN DENSITIES

4.1. Results

The best-fit ionic column densities are listed in Table 1. For the most part, the column densities of the Fe, Si, and Mg ions are of the order of 10^{16} – 10^{17} cm⁻². The column densities of N⁺⁶ and the Ne ions exceed 10^{17} cm⁻², while those of the O ions reach $\sim 10^{18}$ cm⁻².

Comparing these results with those of Sako et al. (2001), we find that the Fe M-shell column densities are consistent. The present column densities for the O K-shell ions are much higher, while those of Fe L-shell are much lower than those of Sako et al. (2001). In order to understand this discrepancy, we went back to the RGS spectrum and compared both data and models with the present spectrum. We conclude that the O K-shell column densities indeed did vary between observations. This can be seen even in our Fig. 1 where features of O^{+6} and O^{+7} , marked by labels, are clearly deeper in the present spectrum, even though the soft excess continuum is higher. Conversely, for all non-oxygen ions, we find that the present ionic column densities obtained from fitting the HETGS spectrum actually reproduce the RGS spectrum fairly well. Other than O, we have no good explanation for the discrepancies with Sako et al. (2001).

Interestingly, we find a relatively high column density of neutral Fe which may not be part of the outflow, as manifested by the $L\alpha$ absorption UTA at 17.53 \AA (see Fig. 3). If we use the solar Fe/H abundance ratio (Asplund et al. 2005), we obtain a neutral gas column density of $N_H \sim 3.5 \times 10^{21} \text{ cm}^{-2}$, much higher than the galactic column $N_H \sim 10^{20} \text{ cm}^{-2}$. This may indicate the presence of neutral gas or dust in the host galaxy reminiscent of the Wills et al. (1992) finding.

4.2. Errors Determination

The column density errors quoted in Table 1 were calculated by keeping an individual ionic column density fixed while performing a minimum $-\chi^2$ fit with all other parameters, and then requiring that $\Delta\chi^2 = 1$ for variations of that individual ionic column density, while all other parameters remain fixed. The more statistically rigorous method would be to require $\Delta\chi^2 = 1$ following a refit of the data. However, since we supplement χ^2 fitting with a more controlled manual fit to the strongest lines, leading to a best fit that is not strictly the χ^2 minimum, this method which involves automatic χ^2 minimization is inapplicable here. Nevertheless, our simpler method gives reliable upper limits to the errors.

For the cases in which the relative error was less than 10%, we assume an error of 10%. The reason is that even for the most prominent lines, we do not trust the column density to better than 10%. Conversely, when the relative error was more than 200%, we quote a nominal error of 200%. In these cases we believe the errors are not statistical.

In §5.1 we need to use symmetrical errors. In order to get a reliable symmetrical error estimate, we introduced one more adjustment. We define a geometrically averaged error :

$$err_{symmetric} = \sqrt{err_{up} \cdot err_{down}}. \quad (4)$$

We use geometrically averaged rather than arithmetically averaged errors, since the geometrical average gives an average in order of magnitude between the two errors, which is the more appropriate value to be applied as a symmetrical error. For the full *AMD* analysis (presented in §5.1), we use the true asymmetrical errors in the manner explained below.

5. ABSORPTION MEASURE DISTRIBUTION

5.1. Method

The large range of ionization states present in the absorber strongly suggests that the absorption arises from gas that is distributed over a wide range of ionization parameter. The total hydrogen column density N_H along the line of sight can therefore be expressed as an integral over its distribution in $\log \xi$. We call this continuous distribution the Absorption Measure Distribution (*AMD* by analogy to the Emission Measure Distribution in emission-line spectra):

$$AMD = dN_H/d(\log \xi) \quad (5)$$

and

$$N_H = \int AMD \, d(\log \xi) \quad (6)$$

The relation between the ionic column densities N_{ion} and the *AMD* is then expressed as:

$$N_{ion} = A_z \int \frac{dN_H}{d(\log \xi)} f_{ion}(\log \xi) d(\log \xi) \quad (7)$$

where N_{ion} is the measured ion column density, A_z is the element abundance with respect to hydrogen assumed to be constant throughout the absorber, and $f_{ion}(\log \xi)$ is the fractional ion abundance with respect to the total abundance of its element. Here, we aim at recovering the *AMD* for IRAS 13349+2438.

As an initial approximation to be relaxed later, let us assume that each ion forms exclusively at the ionization parameter ξ_{max} where its fractional abundance peaks. Furthermore,

if solar abundances A_{Z_\odot} are assumed, the equivalent hydrogen column density can be calculated separately from each ion using the relation:

$$N_H \simeq \frac{N_{ion}}{f_{ion}(\xi_{max})A_{Z_\odot}} \quad (8)$$

and placed at the position of ξ_{max} on an $N_H(\log \xi)$ plot. For this we employed the XSTAR code (Kallman & Krolik 1995) version 2.1kn3 to calculate $f_{ion}(\log \xi)$ using the continuum derived in §3.1 extrapolated to the range of 1 – 1000 Rydberg. The results for IRAS 13349+2438 using solar abundances from Asplund et al. (2005) are presented in Fig. 4. The ions pertaining to each element in the figure are connected by straight lines to guide the eye. The fact that the connecting lines of Fe, Si, Mg, O and Ne largely overlap on this plot implies that the relative abundances of these elements do not deviate much from the solar values. On the other hand, the relative abundance of N and Na appears to be significantly above solar, although there is only one N and one Na ion to show this result. The errors in Fig. 4 are those propagated from the N_{ion} symmetrical uncertainties as explained in the previous section.

The distribution presented in Fig. 4 is only a first approximation for the actual *AMD*. For the real *AMD*, we need to find a distribution $dN_H/d(\log \xi)$ that after integration (eq. 7) will produce all of the measured ionic column densities (Table 1). In fitting for the *AMD* one must take into account the full dependence of f_{ion} on ξ . We assume all charge states see the same ionizing spectrum. This is justified by the absence of significant bound-free absorption edges in the spectrum. All elements are expected to reflect the same *AMD* distribution, due to the assumption that they all reside in the same gas. Iron however, has a special role as it covers almost five orders of magnitude in ξ , more than any other element. Nonetheless, in order to improve the *AMD* fit, we can use other elements as well. In order to incorporate the non-Fe ionic column densities without assuming anything about the elemental abundances, for non-Fe ions we use column density ratios. Using a reference ion for each element (the one with the smallest symmetrical errors), these ratios can be written as:

$$\frac{N_{ion}}{N_{ion-reference}} = \frac{A_z \int \frac{dN_H}{d(\log \xi)} f_{ion}(\log \xi) d(\log \xi)}{A_z \int \frac{dN_H}{d(\log \xi)} f_{ion-reference}(\log \xi) d(\log \xi)} \quad (9)$$

Since there is no *a-priori* physical argument for a specific functional form for the *AMD*, we choose to use a simple staircase function (Fig. 5). The main advantage of this form is the well-localized easily-calculated errors. A similar approach was used for emission by Nordon et al. (2006).

The fit is performed with our Monte-Carlo evolution program in which the only free parameters are the values of the *AMD* in each $\log\xi$ bin. The program receives starting values for each bin, then generates 5000 other *AMD* solutions randomly in the multi-dimensional region around the starting point. For each solution, χ^2 is calculated and the lowest- χ^2 solution is subsequently considered as the new starting point. This process is repeated until χ^2 can not improve any more. In our tests, the program always converged to the same best-*AMD* solution for arbitrary starting values within five orders of magnitude (higher or lower) of the final result. This gives us confidence that the fit finds the global minimum. As this is an ill-defined inversion problem, the *AMD* binning is driven by the correlated errors. At first, we use 10 bins in the range of $\log\xi = -1.25$ to 3.75 (c.g.s.), assuming the *AMD* is zero elsewhere. We then combine bins so that the range and number of bins are optimized so that *AMD* bin values are inconsistent with zero (to within 1σ), except in broad regions of ξ in which the *AMD* is persistently zero. The final number of bins (i.e., the *AMD* resolution) depends on the specific absorber and on the quality of the data, which can limit the bin size.

The *AMD* fit is obtained by the χ^2 minimalization technique with respect to all of the measured Fe N_{ion} values (eq. 7) and N_{ion} ratios of at least one other element (eq. 9). In the calculation of χ^2 , the real asymmetrical errors are used so that when the best-fit *AMD* overestimates an ionic column density, the upper limit error is used and vice versa. For non-Fe ions, the same rule is applied to N_{ion} , while symmetrical errors are used for $N_{ion-reference}$ (eq. 9).

The *AMD* errors are calculated in each bin including correlations between bins. The *AMD* in a given bin is varied from its best-fit value and the whole distribution is refitted. This procedure is repeated until $\Delta\chi^2 = 1$. The fact that changes in the *AMD* in one bin can be compensated by varying the *AMD* in other bins dominates the *AMD* uncertainties. This is what limits the number of bins and the *AMD* resolution. *AMD* in neighboring, excessively narrow bins can not be distinguished by the data, i.e., different distributions produce the measured N_{ion} values to within the errors. A meaningful quantity is the integral of the *AMD* up to ξ (as a function of ξ) since during integration correlated errors cancel out, which explains the small errors on the integrated column density (Fig. 5, bottom panel).

The next step is to estimate the element abundances relative to Fe. This is done by assuming that the other elements are distributed in $\log\xi$ similar to Fe, or in other words, that the *shape* of the *AMD* (e.g., Fig. 5) is manifested in the column density distribution of each and every element. This is what one would expect for a chemically uniform absorber. Indeed, the overlap of elements in Fig. 4 seems to support this assumption. In order to obtain the abundances, we used the *AMD* distribution, by varying the *AMD* normalization to best-fit the column densities of each ion. This single-parameter fit yields for each ion

the relative abundance A_Z/A_{Fe} . The errors on these abundances can be calculated from the $\Delta\chi^2 = 1$ requirement, again using the asymmetrical column density errors, but also the uncertainties on the *AMD* distribution itself. We then average this result for all ions from the same element to obtain our best abundance estimate. The errors on the abundances are calculated by averaging the upward and downward confidence limits separately.

5.2. Results

The best-fit *AMD* for the absorber in IRAS 13349+2438 is presented in Fig. 5. The integrated column density for the absorber of IRAS 13349+2438 is also presented in Fig. 5 in the lower panel. This *AMD* was obtained using 21 ions of Fe and 9 ions of Si. The integrated *AMD* of the absorber in IRAS 13349+2438 (Fig. 5) gives a total column density of $(1.2 \pm 0.3) \times 10^{22} \text{ cm}^{-2}$ compared with $(1-4) \times 10^{22} \text{ cm}^{-2}$ in Sako et al. (2001). The *AMD* features a statistically significant minimum at $0.75 < \log \xi < 1.75$ (c.g.s. units), which corresponds to $4.5 < \log T < 5$ (K) and which was noted also by Sako et al. (2001). This minimum is a manifestation of the relatively low ionic column densities observed for the ions Fe^{+11} – Fe^{+15} seen in Fig. 4 and in Table 1.

In order to check that the observed minimum in the *AMD* of IRAS 13349+2438 is not a result of the S/N, we want to apply the same method to another ionized absorber with a wide range of ionization. The natural choice is the 900 ks HETGS spectrum of NGC 3783. We use the spectrum from Kaspi et al. (2002, Fig. 5), and the same method described above. The results are presented in Figs. 6 and 7 in the same format as for IRAS 13349+2438 (Figs. 4 and 5). The *AMD* of NGC 3783 was obtained using 23 ions of Fe and 4 ions of Ne. Already in Fig. 6, low column densities for the Fe^{+12} – Fe^{+16} and Si^{+9} – Si^{+11} charge states can be seen around $\log \xi \approx 1-2$ (c.g.s. units). Indeed, in the staircase *AMD* reconstruction for NGC 3783 presented in Fig. 7, we find a minimum at $0.75 < \log \xi < 1.75$ (c.g.s. units), which corresponds to $4.5 < \log T < 5$ (K). This minimum is surprisingly similar to that of IRAS 13349+2438, but is more statistically significant and thus better constrained in ξ . We note that a similar minimum has been recently observed in NGC 7469 as well (Blustin et al. 2007).

In Figs. 6 and 7, we include comparisons with the two-component model of Krongold et al. (2003) and the three-component model of Netzer et al. (2003) for the same NGC 3783 HETGS data set. The ionization components of these papers are placed on the plot according to T rather than ξ as different models produce different relations between temperature and ξ . The bin size, is set arbitrarily to $\Delta \log \xi = 0.5$ (c.g.s. units). The column density of each component in those papers then determines the area (height) of its *AMD* contribution in Fig. 7.

It can be seen that all models avoid the region of the *AMD* minimum between $\log\xi \simeq 1$ and 2 (c.g.s. units). On the other hand, only the present method, that allows for a complete distribution, accounts for the full range of absorbing gas from $\log\xi = -1.25$ to $\log\xi = 3.75$ (c.g.s. units). We obtain a total (integrated) N_H value of $(4.1 \pm 0.7) \times 10^{22} \text{ cm}^{-2}$ compared with $(3.8 \pm 1.0) \times 10^{22} \text{ cm}^{-2}$ and $(2.0 \pm 0.8) \times 10^{22} \text{ cm}^{-2}$ obtained by Netzer et al. (2003) and by Krongold et al. (2003), respectively. Note, that we use slightly different solar abundances than the other authors do.

Finally, the results for the chemical abundances obtained for both IRAS 13349+2438 and NGC 3783 using the method described in the previous section are listed in Table 2. We include in the table only elements with at least two significant ion detections. In both AGNs the Ne/Fe, Mg/Fe and O/Fe abundance ratios are slightly above or at about their solar value. The Si/Fe ratio is above solar. The S/Fe ratio can be measured only for NGC 3783 where it is at its solar value. In general we can say that in both AGNs the metal abundances are approximately consistent with solar values.

5.3. Discussion: Observing Thermal Instability

The extent to which we can describe the low ionization region of the *AMD* strongly depends on the photoionization balance, which is highly uncertain at low- ξ for two main reasons. First, the uncertainties in the dielectronic recombination rates of the low charge states of Fe at low (photoionized) temperatures are well known to be severely underestimated in all codes including XSTAR; see Netzer (2004) and recently Badnell (2006). Correcting these would shift the ionization balance at a given ξ value towards lower charge states, which would result in a more compact *AMD* not extending as far on the low- ξ end. The other effect that could drastically change our low- ξ *AMD* is photoionization of the low charge states by the EUV and UV continuum, which is only poorly constrained. For example, a softer continuum than we assumed here (see §3.1), would allow for more highly ionized M-shell charge states at a given ξ value. Consequently, it is important to understand that the exact position of the low- ξ peak of the *AMD* for both IRAS 13349+2438 and NGC 3783 is only poorly constrained, and will depend on the combined correction for the DR rates and for the soft continuum. Conversely, the total column density in this component as well as the existence of a minimum in the *AMD* are robust.

One explanation that comes to mind for the minimum observed in the *AMD* of both IRAS 13349+2438 and NGC 3783 is thermal instability. If photoionized gas is thermally unstable at these temperatures, it would provide a natural explanation for the absence of absorption and for the low column densities of the charge states that form primarily at these

temperatures. Note that our *AMD* binning is driven by the requirement for meaningful errors. Consequently, we can not determine where the alleged instability occurs to better accuracy than the ξ and T regimes given above, as narrower bins will inevitably result in excessive *AMD* uncertainties. The resulting *AMD* distributions presented in Figs. 5 and 7 along with their similar minima are reminiscent of what is widely referred to in the literature as the two-phase models of gas in photoionization equilibrium (Krolik et al. 1981). These models have been invoked for AGN most importantly to allow for the confinement of low- T high-density clouds by high- T diffused gas. It is important to stress that the currently derived *AMD* is not a model. It represents a direct measurement of the ionization structure of the absorber that is more complete and more detailed than a multi iso- ξ fit. To that end, the observed *AMD* minima provide direct evidence for a thermal unstable temperature region that can not be obtained from iso- ξ fits.

The observed minimum or two-phase structure can also be ascribed to two geometrically distinct regions along the line of sight, a high ionization region and a low ionization region, both which have their own gaussian like *AMD* distribution. However, there are good reasons to believe that gas at $4.5 < \log T < 5$ (K) would be unstable as the cooling function $\Lambda(T)$ is generally decreasing in this temperature regime (Krolik et al. 1981). Additionally, the model of Netzer et al. (2003, Fig. 12) for NGC 3783 shows that this region is marginally unstable. The model of Gonçalves et al. (2006) for NGC 3783 avoids temperature zones, which could be a result of thermal instability. Interestingly, the avoided region at $4.5 \lesssim \log T \lesssim 5$ (K) is consistent with the present measurement. However, there is another region of avoidance in that model at $5.3 \lesssim \log T \lesssim 6$ (K) that our measurement does not show. The model of Krongold et al. (2003) has a very wide unstable region at $5.3 \lesssim \log T \lesssim 7.5$. However, both Netzer et al. (2003) and Krongold et al. (2003) find an absorption component in this temperature regime, as we do. As the regions of instability depend strongly on unobserved regions of the ionizing spectra, the theoretical stability analysis models have to be treated with caution.

6. CONCLUSIONS

We have analyzed the thermal and chemical structure of the ionized outflow in the quasar IRAS 13349+2438. Using a new *AMD* reconstruction method, we measure the distribution of column density in the outflow as a function of ξ . We find a double-peaked distribution with a significant minimum at $0.75 < \log \xi < 1.75$ (c.g.s. units), which corresponds to temperatures of $4.5 < \log T < 5$ (K). Using a comparison method of the *AMD* derived for different elements we are able to estimate the relative chemical abundances in the outflow.

We find that all of the abundances relative to Fe are more or less solar. For comparison, we applied the same analysis to the excellent-quality X-ray spectrum of NGC 3783. We find a similar minimum in the *AMD* and rather similar abundances suggesting perhaps that these could be common features in AGN outflows. We believe this minimum is due to thermal instability.

This research was supported by grant #28/03 from the Israel Science Foundation, by a grant from the Asher Space Research Institute at the Technion. S.K. acknowledges support of the Zeff fellowship at the Technion.

REFERENCES

- Asplund, M., Grevesse, N., & Sauval, J., A. 2005, APS Conference Series , Vol. XXX , astro-ph/0410214 Oct 2004
- Arav, N. , Becker, R. H. , Laurent-Muehleisen, S. A. , Gregg, M. D. , White, R. L. , Brotherton, M. S. , & de Kool, M. 1999, ApJ, 524, 566
- Badnell, N. R. 2006, ApJ, 651, L73
- Bar-Shalom, A., Klapisch, M., & Oreg, J. 2001, J. Quant. Spectr. Radiat. Transfer, 71, 169
- Behar E., Cottam J C., & Kahn S. M. 2001, ApJ, 548, 966
- Behar, E., Sako, M., & Kahn S. M. 2001, ApJ, 563, 497
- Behar, E., Rasmussen, A. P., Blustin, A. J., Sako, M., Kahn, S. M., Kaastra, J. S., Branduardi-Raymont, G., & Steenbrugge, K. C. 2003, ApJ, 598, 232
- Blustin, A. J., et al. (2007), A&A, in press (astro-ph/0702311)
- Brandt, W. N., Fabian, A. C., & Pounds, K. A. 1996, RAS 278 , 326
- Brandt, W. N., Mathur, S., Reynold, C. S., & Elvis, M. 1997, MNRAS, 292, 407
- Brinkman, A. C., Kaastra, J. S., van der Meer, R. L. J., Kinkhabwala, A., Behar, E., Kahn, S. M., Paerels, F. B. S., & Sako, M. 2002, A&A, 396, 761
- Costantini et al. 2007, A&A, 461, 121
- Crenshaw, D. M., Kraemer, S. B., & George, I. M., 2003, ARA&A, 41, 117
- Gonçalves, A. C , Collin, S., Dumont, A.-M., Mouchet, M., Rózańska, A., Chevallier, L., & Goosmann, R. W. 2006, A&A, 451, 23
- Gu, M. F., Holczer, T., Behar, E., & Kahn, S. M. 2006, ApJ, 641, 1227
- Holczer, T., Behar, E., & Kaspi, S. 2005, ApJ, 632, 788
- Kallman, T. R., & Krolik, J. H. , XSTAR - A Spectral Analysis Tool, HEASARC, NASA/GSFC, Greenbelt. 1995
- Kaastra, J. S. Steenbrugge, K. C., Raassen, A. J. J., van der Meer, R. L. J., Brinkman, A. C., Liedahl, D. A., Behar, E., & de Rosa, A. 2002, A&A , 386, 427

- Kaspi et al. 2001, ApJ, 554, 216
- Kaspi, S. & Behar, E. 2006, ApJ, 636, 674
- Kaspi et al. 2002, ApJ, 574, 643
- Kim, D. C., Sanders, D. B., Veilleux, S., Mazzarella, J. M., & Soifer, B. T. 1995, ApJS, 98, 129
- Krolik, J. H., McKee, C. F., & Tarter, C. B. 1981, ApJ, 249, 422
- Krongold, Y., Nicastro, F., Brickhouse, N. S., Elvis, M., Liedahl, D. A., & Mathur, S. 2003, ApJ, 597, 832
- Murphy, E. M., Lockman, F. J., Laor, A., & Elvis, M. 1996, ApJS, 105, 369
- Netzer, H., et al. 2003, ApJ, 599, 933
- Netzer, H. 2004, ApJ, 604, 551
- Nordon, R., Behar, E. , & Güdel, M. 2006, A&A, 446, 621
- Sako, M. et al. 2001, A&A, 365, L168
- Siebert, J., Komossa, S., & Brinkmann, W. 1999, A&A, 351, 893
- Steenbrugge, K. C. et al. 2005 , A&A, 432, 453
- Wills, B. J., Wills, D., Evans N. J. II, Natta, A., Thompson, K. L., Breger, M., & Sitko, M. L. 1992 , ApJ, 400, 96

Table 1. Best-fit column densities for ions detected in the 2004 HETGS spectrum of IRAS 13349+2438 and comparison to the 2000 RGS observation (Sako et al. 2001).

Ion	HETGS Column Density (10^{16} cm^{-2})	RGS Column Density (10^{16} cm^{-2})	Ion	HETGS Column Density (10^{16} cm^{-2})	RGS Column Density (10^{16} cm^{-2})
N ⁺⁶	45^{+21}_{-23}	13^{+8}_{-4}	Fe ⁺⁰	$9.9^{+3.0}_{-5.2}$...
O ⁺³	30^{+21}_{-18}	...	Fe ⁺³	$1.3^{+2.2}_{-1.3}$...
O ⁺⁴	$40^{+5.0}_{-36}$...	Fe ⁺⁴	$1.0^{+1.6}_{-1.0}$...
O ⁺⁵	$15^{+30}_{-3.3}$...	Fe ⁺⁵	$1.9^{+0.8}_{-1.9}$...
O ⁺⁶	$78^{+14}_{-8.0}$	$3.7^{+2.7}_{-1.8}$	Fe ⁺⁶	$2.0^{+0.7}_{-2.0}$	$1.5^{+1.5}_{-1.3}$
O ⁺⁷	140^{+21}_{-39}	$9.5^{+8.7}_{-4.7}$	Fe ⁺⁷	$2.7^{+0.8}_{-2.7}$	$4.6^{+1.5}_{-1.3}$
Ne ⁺⁶	$2.7^{+3.3}_{-2.1}$...	Fe ⁺⁸	$1.8^{+0.9}_{-1.3}$	$0.9^{+1.2}_{-0.9}$
Ne ⁺⁷	$5.5^{+3.6}_{-3.0}$...	Fe ⁺⁹	$2.5^{+0.8}_{-2.3}$	$2.4^{+1.3}_{-1.1}$
Ne ⁺⁸	$22^{+35}_{-2.2}$	120^{+50}_{-60}	Fe ⁺¹⁰	$2.0^{+0.9}_{-1.8}$	$1.9^{+1.1}_{-0.9}$
Ne ⁺⁹	$16^{+12}_{-6.7}$	49^{+100}_{-32}	Fe ⁺¹¹	$1.4^{+1.2}_{-1.4}$	$6.4^{+10}_{-4.4}$
Na ⁺¹⁰	$7.0^{+3.0}_{-3.2}$...	Fe ⁺¹²	$0.2^{+0.4}_{-0.2}$...
Mg ⁺⁴	$2.0^{+4.0}_{-2.0}$...	Fe ⁺¹³	$2.0^{+0.4}_{-2.0}$...
Mg ⁺⁵	$8.0^{+4.3}_{-5.0}$...	Fe ⁺¹⁴	$0.4^{+0.8}_{-0.4}$...
Mg ⁺⁶	$6.2^{+1.8}_{-5.5}$...	Fe ⁺¹⁵	$0.8^{+0.6}_{-0.8}$...
Mg ⁺⁷	$4.6^{+1.6}_{-3.8}$...	Fe ⁺¹⁶	$2.7^{+1.2}_{-1.1}$	17^{+16}_{-12}
Mg ⁺⁸	$4.4^{+1.2}_{-2.3}$...	Fe ⁺¹⁷	$2.7^{+0.4}_{-2.0}$	63^{+24}_{-19}
Mg ⁺⁹	$2.8^{+1.4}_{-2.0}$...	Fe ⁺¹⁸	$2.8^{+0.8}_{-1.9}$	97^{+48}_{-39}
Mg ⁺¹⁰	$5.5^{+2.0}_{-1.6}$...	Fe ⁺¹⁹	$2.5^{+0.7}_{-1.6}$	30^{+28}_{-20}
Mg ⁺¹¹	$1.0^{+2.0}_{-1.0}$...	Fe ⁺²⁰	$0.5^{+0.9}_{-0.5}$...
Si ⁺⁵	$15^{+2.7}_{-15}$...	Fe ⁺²¹	$1.6^{+2.6}_{-1.0}$...
Si ⁺⁶	$5.0^{+3.7}_{-5.0}$...	Fe ⁺²²	$5.0^{+0.7}_{-5.0}$...
Si ⁺⁷	$7.0^{+3.3}_{-3.4}$...	Fe ⁺²³	$8.0^{+3.7}_{-4.0}$...
Si ⁺⁸	$7.0^{+2.6}_{-3.2}$...	Ni ⁺¹⁸	$0.6^{+0.7}_{-0.4}$...
Si ⁺⁹	$4.9^{+2.6}_{-2.0}$...			
Si ⁺¹⁰	$1.7^{+1.3}_{-1.3}$...			
Si ⁺¹¹	$3.0^{+2.9}_{-1.3}$...			
Si ⁺¹²	$5.0^{+10}_{-0.5}$...			
Si ⁺¹³	$8.0^{+15}_{-1.6}$...			

Table 2. Relative abundances with respect to Fe in the ionized X-ray absorbers of IRAS 13349+2438 and NGC 3783, compared with solar ratios (Asplund et al. 2005)

Element	Solar Ratios (A_Z/A_{Fe}) $_{\odot}$	IRAS 13349+2438 (A_Z/A_{Fe})	NGC 3783 (A_Z/A_{Fe})	IRAS 13349+2438 (A_Z/A_{Fe})/(A_Z/A_{Fe}) $_{\odot}$	NGC 3783 (A_Z/A_{Fe})/(A_Z/A_{Fe}) $_{\odot}$
O (5,5) ^a	16.2 ± 2.6	$21.1^{+6.8}_{-6.9}$	$16.5^{+2.2}_{-2.3}$	$1.3^{+0.5}_{-0.5}$	$1.0^{+0.2}_{-0.2}$
Ne (4,4)	2.5 ± 0.4	$3.3^{+3.9}_{-1.0}$	$3.5^{+0.8}_{-1.9}$	$1.3^{+1.6}_{-0.4}$	$1.4^{+0.3}_{-0.8}$
Mg (8,9)	1.2 ± 0.3	$1.7^{+0.6}_{-0.6}$	$1.9^{+0.3}_{-0.7}$	$1.4^{+0.5}_{-0.5}$	$1.5^{+0.4}_{-0.7}$
Si (9,9)	1.1 ± 0.2	$2.6^{+1.0}_{-0.8}$	$2.1^{+0.2}_{-0.6}$	$2.3^{+0.8}_{-0.7}$	$1.9^{+0.2}_{-0.6}$
S (0,2)	0.5 ± 0.1	...	$0.5^{+0.1}_{-0.2}$...	$1.0^{+0.2}_{-0.5}$

^aNumber in parenthesis indicate the number of ions used for each element, respectively for IRAS 13349+2438 and for NGC 3783 in the determination of the abundances.

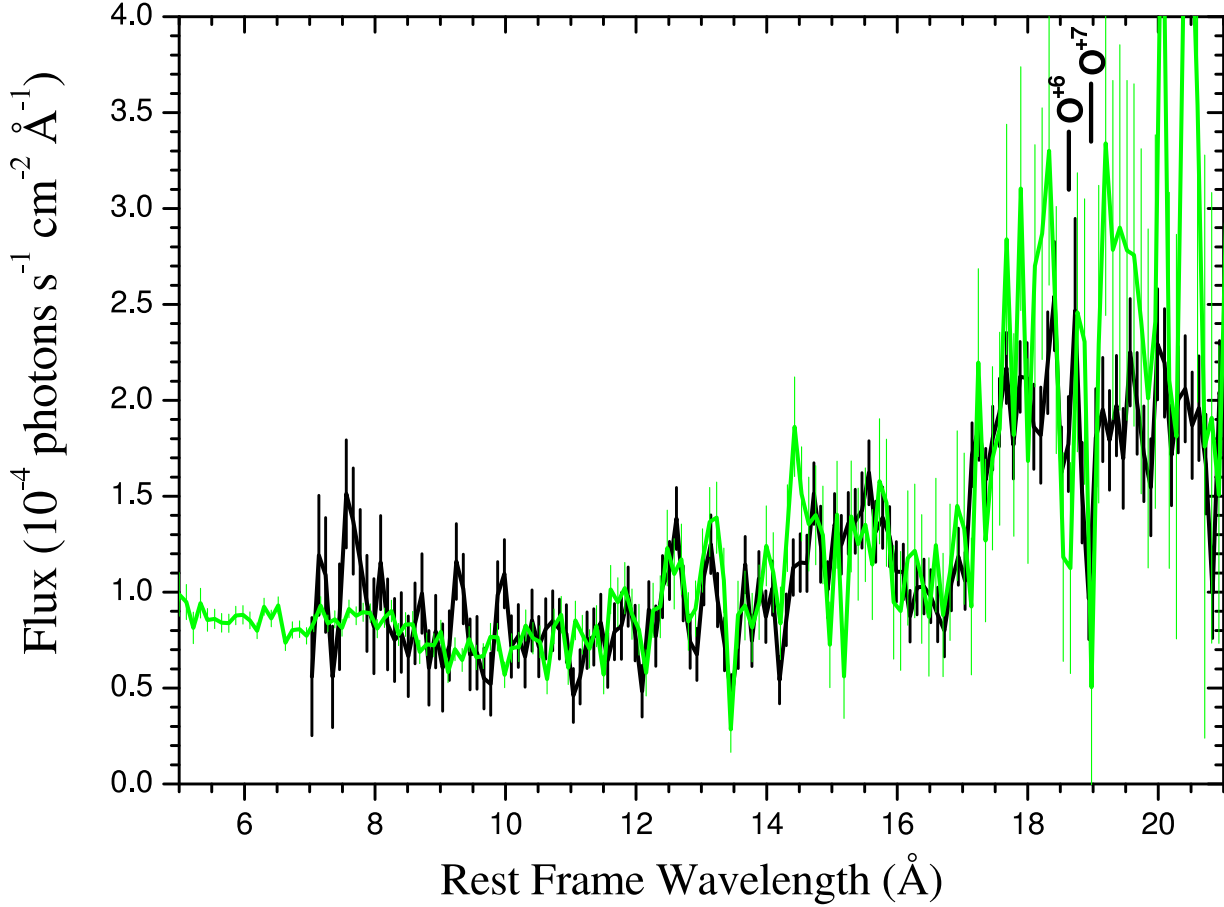


Fig. 1.— The present HETGS spectrum of IRAS 13349+2438 (in green) observed on 22–26 February, 2004 compared to the RGS spectrum (in black) observed on 19–20 June, 2000. Despite the ~ 4 years difference, the flux level of the two observations appears almost unchanged, especially the hard X-Ray region and up to 17 Å. There is noticeable variability beyond 17 Å. Two O line locations are marked to demonstrate the absorption variability of oxygen.

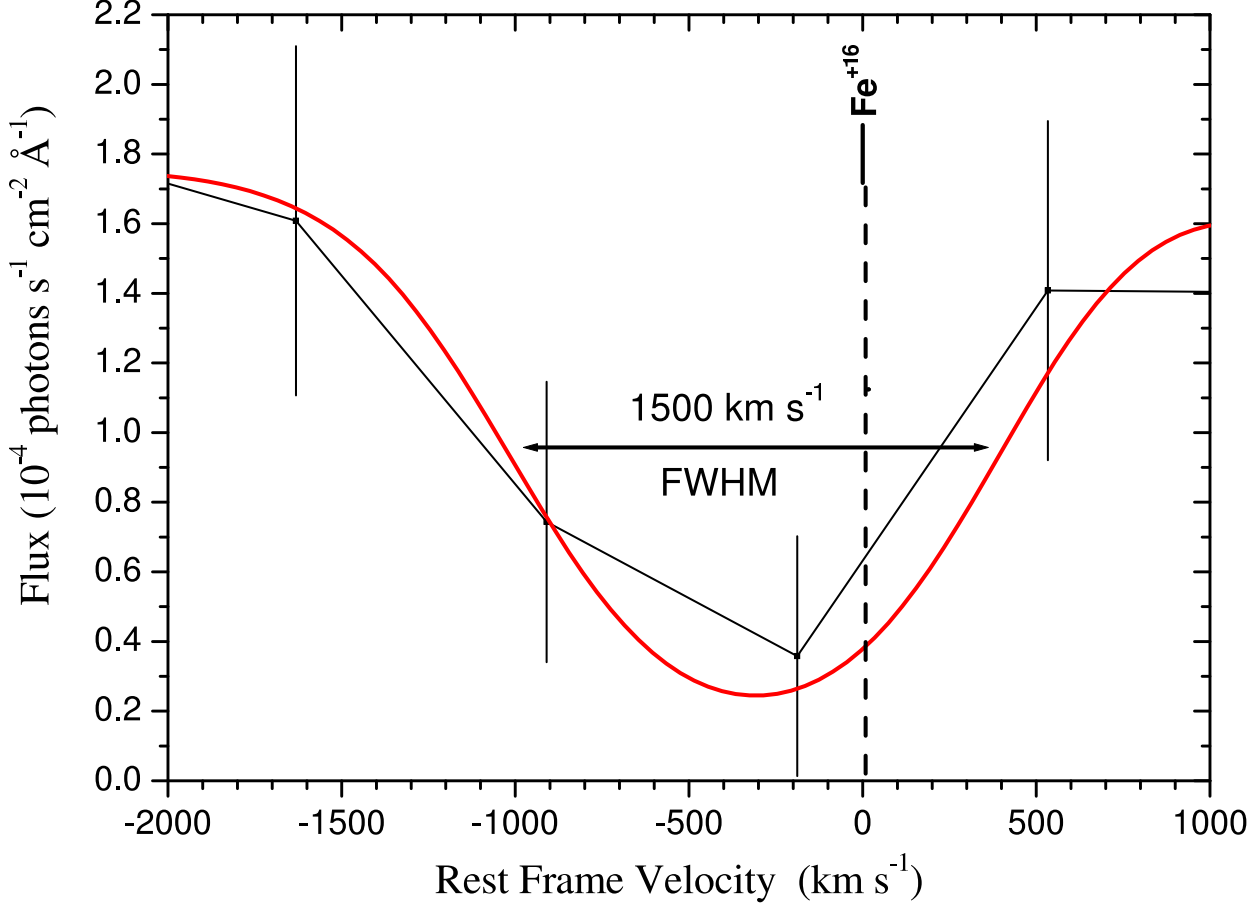


Fig. 2.— Profile of the strong, isolated Fe^{+16} absorption line at 15.01 \AA plotted in velocity space with the best-fit profile in red. The global best-fit position of $-300\ km\ s^{-1}$ (blue-shift) and best-fit broadening corresponding to FWHM of $1500\ km\ s^{-1}$ ($v_{turb} = 640\ km\ s^{-1}$) are demonstrated.

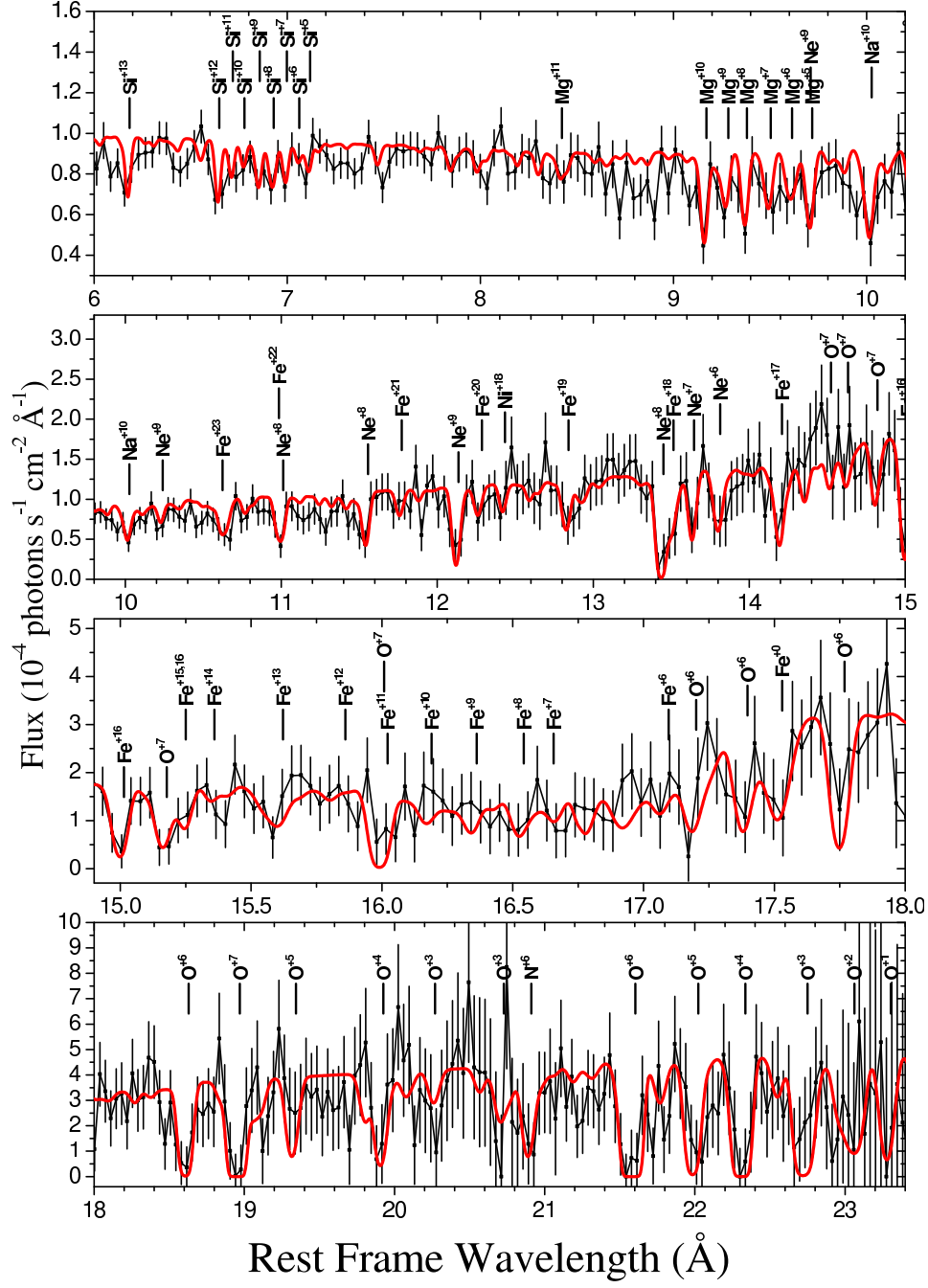


Fig. 3.— *Chandra* HETGS spectrum of IRAS 13349+2438 corrected for cosmological redshift ($z = 0.10764$). The red line is the best-fit model in which a blue-shift velocity of -300 km s^{-1} was applied to all ions. Ions responsible for the strongest lines and blends are marked above the data.

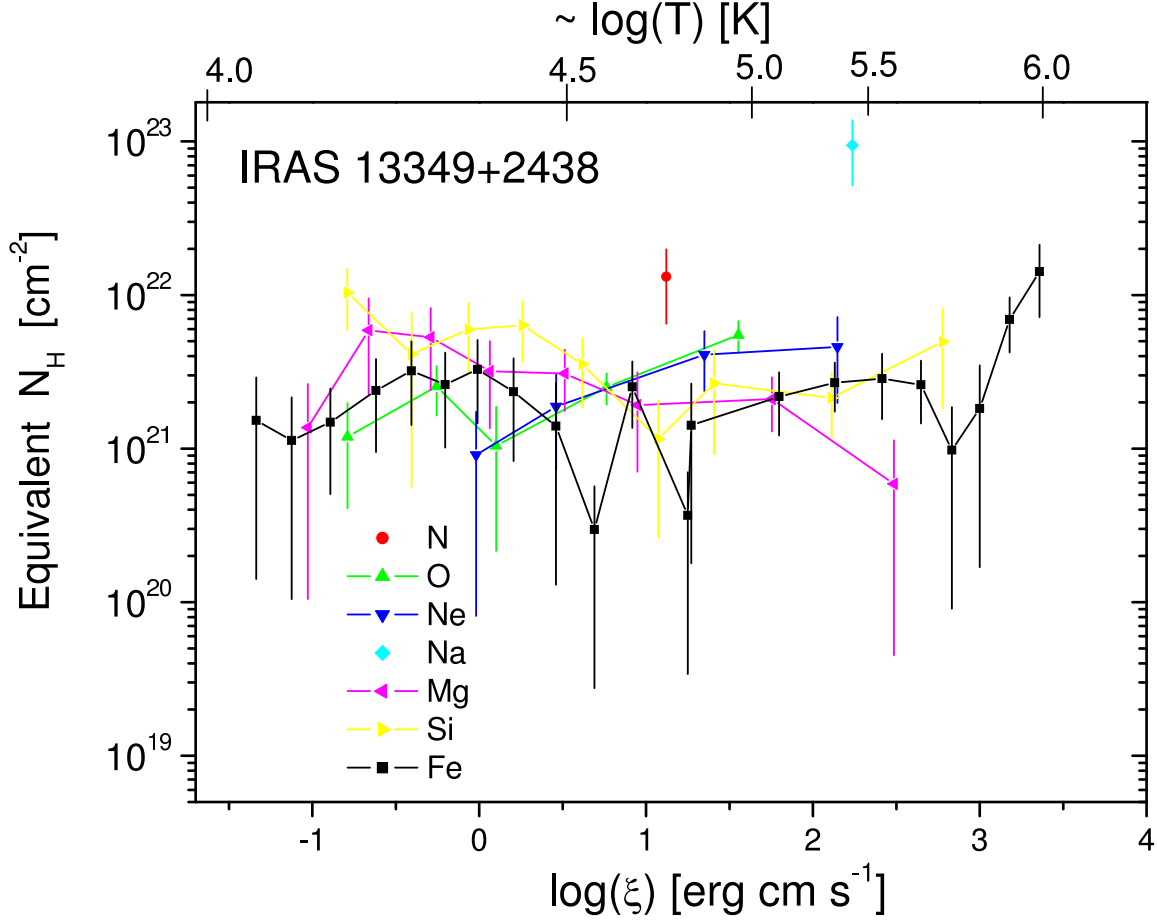


Fig. 4.— Equivalent N_H distribution (eq. 8) obtained for the IRAS 13349+2438 outflow assuming ions form at ξ_{max} and assuming solar abundances (Asplund et al. 2005). Lines are drawn between data points just to guide the eye. Vertical offsets between elements indicate deviations from solar abundances. The corresponding temperature scale, obtained from the XSTAR computation is shown at the top of the figure.

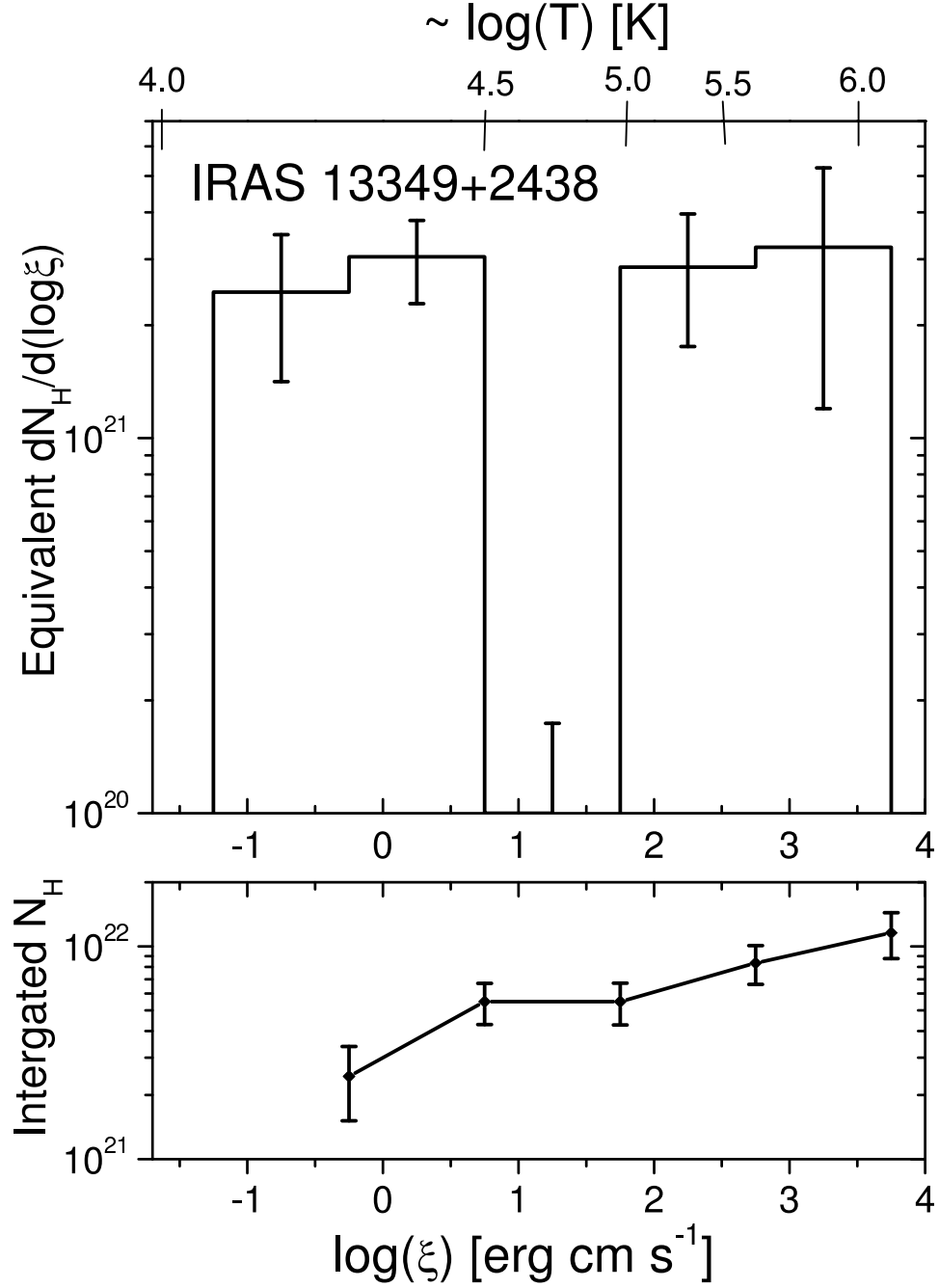


Fig. 5.— *AMD* of IRAS 13349+2438 scaled by the solar Fe/H abundance 2.82×10^{-5} . The corresponding temperature scale, obtained from the XSTAR computation is shown at the top of the figure. The third bin value is zero, so only an upper limit error was calculated. Note the minimum at $0.75 < \log \xi < 1.75$ (c.g.s. units) corresponding to $4.5 < \log T < 5$ (K). The integrated column density up to ξ is shown in the lower panel yielding a total of $N_H = (1.2 \pm 0.3) \times 10^{22} \text{ cm}^{-2}$.

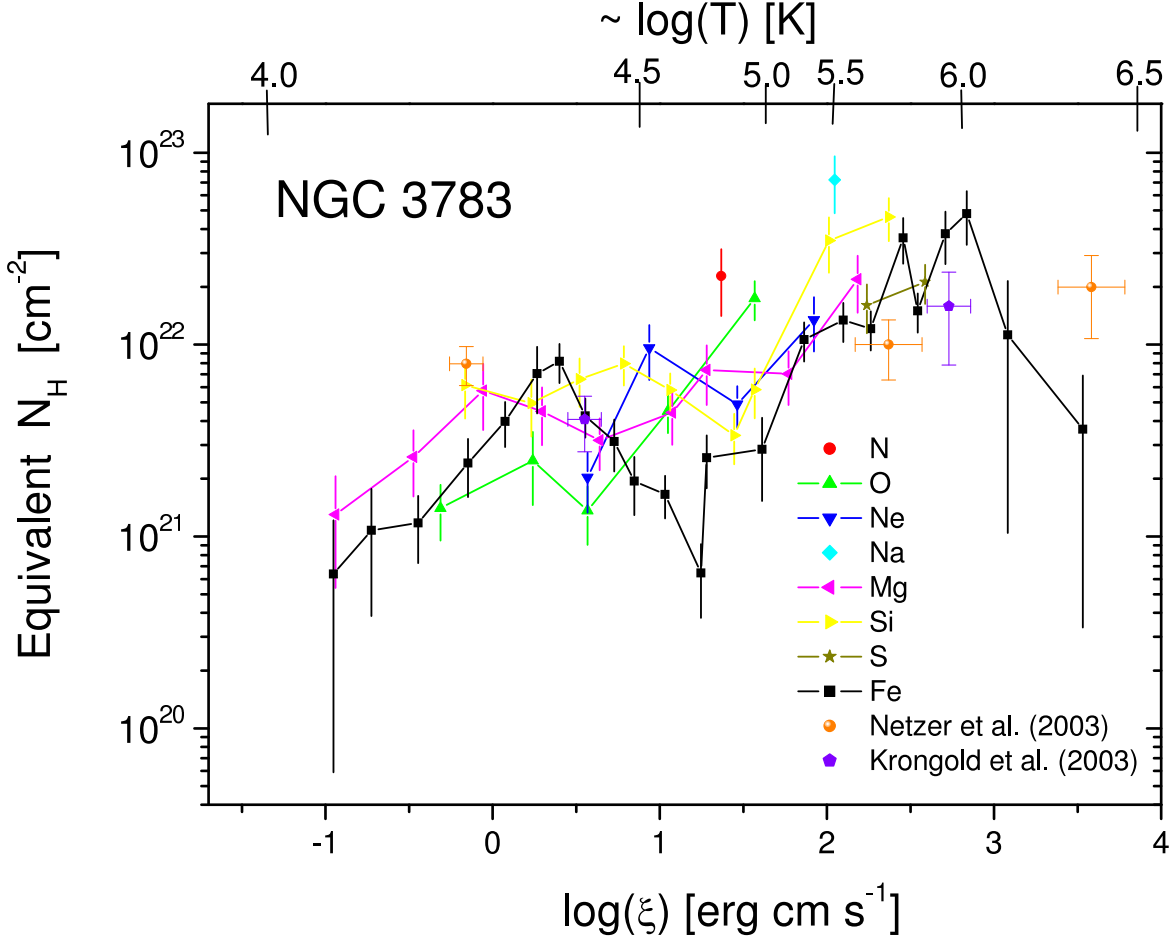


Fig. 6.— Equivalent N_H distribution (eq. 8) obtained for the NGC 3783 outflow assuming ions form at ξ_{max} and assuming solar abundances (Asplund et al. 2005). Lines are drawn between data points just to guide the eye. Vertical offsets between elements indicate deviations from solar abundances. The corresponding temperature scale, obtained from the XSTAR computation is shown at the top of the figure. The Netzer et al. (2003) three component model results and the Krongold et al. (2003) two component model results are plotted for comparison.

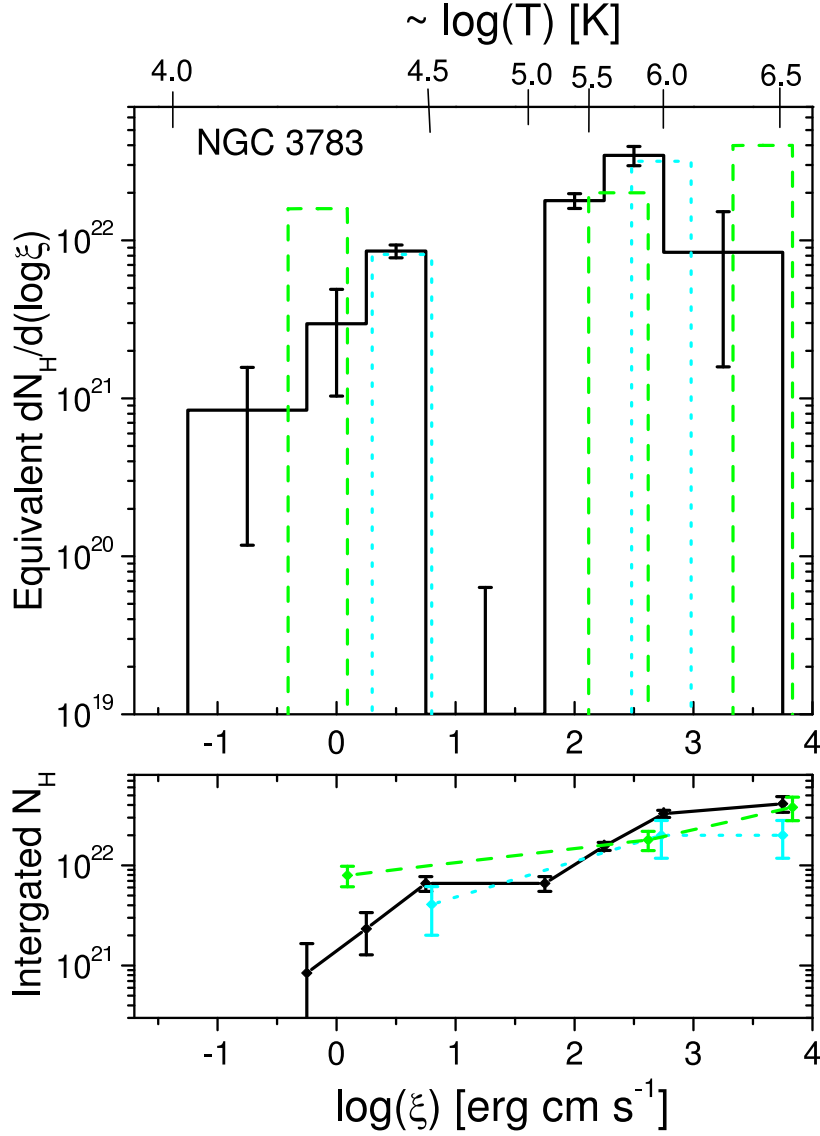


Fig. 7.— *AMD* of NGC 3783 scaled by the solar Fe/H abundance of 2.8×10^{-5} . The corresponding temperature scale, obtained from the XSTAR computation is shown at the top of the figure. Note the minimum at $0.75 < \log \xi < 1.75$ (c.g.s. units) corresponding to $4.5 < \log T < 5$ (K), a behavior similar to that of IRAS 13349+2438, but better constrained here. The fourth bin value is zero so only an upper limit error is calculated. The integrated column density up to ξ is shown in the lower panel yielding a total of $N_H = (4.1 \pm 0.7) \times 10^{22}$ cm $^{-2}$. Green dashed and cyan dotted lines represent the three- and two- components results, respectively, of Netzer et al. (2003) and of Krongold et al. (2003) where each component is broadened arbitrarily to $\Delta \log \xi = 0.5$ (c.g.s. units) bins.